

A review of the structure and dynamics of nanoconfined water and ionic liquids via molecular dynamics simulation

Masumeh Foroutan^a, S. Mahmood Fatemi, and Farshad Esmaeilian

Department of Physical Chemistry, School of Chemistry, College of Science, University of Tehran, Tehran, Iran

Received 15 June 2016 and Received in final form 18 November 2016

Published online: 24 February 2017 – © EDP Sciences / Società Italiana di Fisica / Springer-Verlag 2017

Abstract. During the past decade, the research on fluids in nanoconfined geometries has received considerable attention as a consequence of their wide applications in different fields. Several nanoconfined systems such as water and ionic liquids, together with an equally impressive array of nanoconfining media such as carbon nanotube, graphene and graphene oxide have received increasingly growing interest in the past years. Water is the first system that has been reviewed in this article, due to its important role in transport phenomena in environmental sciences. Water is often considered as a highly nanoconfined system, due to its reduction to a few layers of water molecules between the extended surface of large macromolecules. The second system discussed here is ionic liquids, which have been widely studied in the modern green chemistry movement. Considering the great importance of ionic liquids in industry, and also their oil/water counterpart, nanoconfined ionic liquid system has become an important area of research with many fascinating applications. Furthermore, the method of molecular dynamics simulation is one of the major tools in the theoretical study of water and ionic liquids in nanoconfinement, which increasingly has been joined with experimental procedures. In this way, the choice of water and ionic liquids in nanoconfinement is justified by applying molecular dynamics simulation approaches in this review article.

1 Introduction

Confined systems have been of wide interest in recent years because of their different properties in comparison with bulk systems [1–4]. These systems have been the topic of broad research, particularly as a result of their potential applications for the development of new nanoscale devices. The term “confined geometry” is used to describe the confinement of molecular systems inside the pores with dimensions comparable to the size of the confined molecule. Surface interactions caused by low dimensionality and spatial restriction of the confining matrix result in a different chemical and physical behavior of the confined systems in comparison with the bulk systems [5]. Various types of nano matrices have been taken for confinement, such as MCM-41 [6], SBA-15 [7], zeolites [8], carbon nanotubes [9], boron nitride nanotube [10], reverse micelles [11], clays [12], fullerenes [13], graphene [14], graphene oxide [15], etc. [16–18].

The awareness of the relation between nanoscopic confinement and the behavior of water has drawn tremendous interest of researchers. This is relevant to different phenomena and systems in biology, such as permeability of ion channels and protein stability. In chemistry and chemical engineering, it is related to the nano-fluidic devices and

molecular sieves and in geology it is relevant to transport through porous rocks. Other areas of technology and science are also influenced by this impact [19]. Depending on the confinement dimensions, the cavity surface, and also pressure and temperature, the state of the confined water and its physical properties have been proven to be widely varied. Therefore, numerous efforts in recent years focused on extensive investigation on the physical and chemical properties of confined water [20]. It has been shown that the highly unusual properties of confined water originate from the weak interaction with the confining wall combined with the local ordering of the hydrogen bonding network imposed by the confinement [21]. Confined water can thus have different structure, dynamics, and phase diagram than bulk water [22,23].

On the other hand, ionic liquids (ILs) [24,25] as new designing materials have been recently considered as an alternative solvent with many interesting qualities. For many of the electrochemical applications, ILs are promising for supercapacitors [26], batteries [27], and solar cells [28]. Therefore, it is important to have a fundamental understanding about the characteristics of the confined ILs for various applications such as electrolytes in energy devices, lubricants or surface modifiers and solvents for nanoparticle dispersion and colloidal materials [29].

Investigations of the interfaces of the ILs have been carried out using experimental study, for example a

^a e-mail: foroutan@khayam.ut.ac.ir

number of experimental techniques, including NMR [30], small-angle X-ray and neutron scattering [31], X-ray photoelectron spectroscopy [32] have been used to investigate the properties of fluids confined in nanopores, but a detailed interpretation of the experimental results is often difficult, since direct evidence of the structures is not trivial to obtain and different experiments have led to contradictory conclusions. Computer simulations are a convenient tool to study the water and ILs in nanoconfinement [33,34] because they can give a microscopic picture of the process [35]. They avoid some of the experimental difficulties associated with the observation of the structures and ultimately afford a theoretical understanding of the effects that play a role in water and ILs in nanoconfinement [36]. In this paper, attempt has been made to review advances in molecular dynamic studies of nanoconfined water and ILs, particularly at carbon nanotubes, graphene, graphene oxide, etc. We believe that the purpose of a review is to identify leading concepts in the field and main results for the system of interest.

2 Nanoconfinement of water

In this section, we discuss the structure of water in a narrow and large confinements, respectively. After analyzing the structure of confined water in carbon nanotube, graphene and their derivations, other nano matrices will be discussed.

To understand various nano-scaled technological systems, it is crucial to know the behavior of water confined in diverse geometries, with length scales similar to that of its diameter. In these confined regions, the dynamics and structure of water is noticeably distinct from bulk water [37]. The molecular motion of water molecules, which is related to the distance of the latter from the confining walls, will modify the properties of the nano water confined. In order to understand the characteristics of confined water, it has been the subject of extensive research. For example, surface water has been shown to play an important role in passivation, electrochemistry and corrosion chemistry as well as in catalysis [38]. Confined water has been found to have a key role in transport phenomena in environmental sciences [39]. It is worth mentioning here that in the absence of confined water, the chemistry of aerosols in both organic and inorganic fields would be defective [40]. Apart from the aforementioned observations, perhaps the most significant observation is that the biological response of materials can be influenced by the physicochemical properties of confined water [41].

2.1 Confinement within carbon nanotube and its derivations

A carbon nanotube (CNT) is one such novel material for nanoconfined water [42]. Although nanotubes are hydrophobic and have a tendency to aggregate [43–49], experimental studies on CNTs have revealed that water can

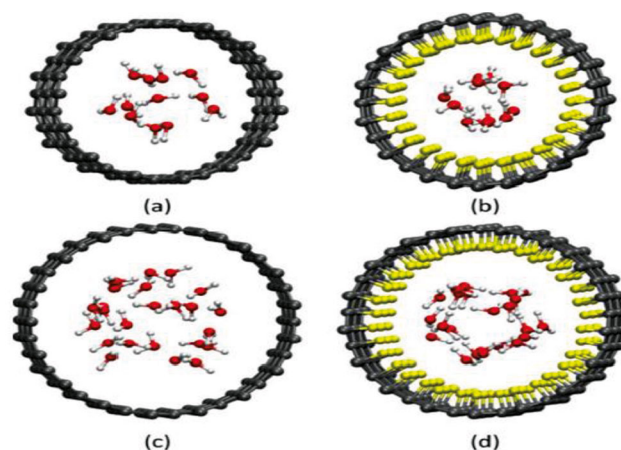


Fig. 1. CNT+H₂O systems used in this study: (a) N-14, (b) F-14, (c) N-17, and (d) F-17. The nomenclature N-14 and N-17 will be used for the non-fluorinated CNTs and F-14 and F-17 for the fluorinated CNTs. The different colored spheres represent different atom types, where gray is carbon, red oxygen, white hydrogen, and yellow fluorine, Reprinted with permission from ref. [56], © (2015), with permission from Royal Society of Chemistry.

be confined in open-ended CNTs [50,51], as well as theoretical/computational calculations [52]. Other theoretical studies have been used to clarify water structures, including hydrogen bonding inside CNTs [53]; for example, Jena *et al.* have found that the factors of confinement length scale and the local nanoscale curvature were highly effective in governing the electronic and structural properties of water molecule presented inside the CNT in a general manner [54]. There seems to be an interaction between confinement and curvature which determines the electronic properties of water in nanoconfinement. In another study, Zhang *et al.* have used MD simulations to investigate the mutual effects of confinement and surface of CNTs on the temperature-dependent water diffusion [55]. They found that the two features of CNTs, the nanoscale surface and the small confinement, can induce anomalous diffusion behaviors in the water. The diffusion coefficient of the confined water molecules was found to show a non-monotonic dependence on the confinement size along with an unexpected increase inside the large CNTs compared to that of bulk water. In another approach, Clark II and Paddison have investigated the effect of nanoscale confinement on the dynamical and structural properties of water using *ab initio* MD simulations [56]. The authors have employed CNTs with two different diameters (11.0 and 13.3 Å) as confinement vessels. Furthermore, to investigate the effect of the confined environment on the determined properties, the inner walls of the CNTs were either fluorinated or left bare. Representative images of the systems are shown in fig. 1.

It was observed that the water molecules were preferentially localized close to the surface of CNTs and exhibited highly ordered structures in the fluorinated nanotubes while those in the bare CNTs were more randomly dispersed. Also, weak interactions which resembled hydrogen

bondings between the fluorine atoms and water molecules were observed. These interactions happened at a higher frequency in the smaller diameter CNTs indicating the effect of the confinement dimensions on these interactions. Also, the water occupancy of open-ended zigzag and armchair CNTs immersed in water, with a length of ≈ 10 nm and diameters from 0.54 nm and 2.7 nm was investigated by Li and Schmidt [57]. They used MD simulations for SPC, SPCE, TIP3P, TIP4P, and TIP5P water models, and concluded that there is only a minor influence resulting by the details of the water-water interaction. In addition, it was found that the anisotropy parameter of the water-carbon interaction is not an effective factor either.

Water structure inside CNT initiates single-file water than more bulk-like confined water. In this regard, Maiti *et al.* have shown that the water molecules inside the CNT show solid-like ordering at room temperature [58]. They have pointed out that the water molecules undergo normal mode diffusion and not subdiffusion inside these short, open-ended CNTs. As the geometric constraints would have suggested, there is a strong correlation due to hydrogen bonding between neighboring water molecules. They have found that if the particles inside the channel interact sufficiently strong with one another and form a single correlated cluster, then their mode of diffusion would be normal (Fickian) instead of single file even if the particles cannot cross one another. This is probably the reason for observing normal mode diffusion in a recent MD simulation of water molecules in a narrow CNT [59]. The size of the nanotube allows only a single file of water molecules inside the nanotube. To observe single file diffusion in such a system, the parameters (interaction strength, temperature, length of the channel, etc.) must be such that the particles inside the channel form several clusters.

MD simulations demonstrated that water spontaneously fills the hydrophobic cavity of a CNT. To gain a quantitative thermodynamic understanding of this phenomenon, Maiti *et al.* have shown that the increase in energy of a water molecule inside the nanotube is compensated by the gain in its rotational entropy [60]. The confined water is in equilibrium with the bulk water and the Helmholtz free energy per water molecule of confined water is the same as that in the bulk within the accuracy of the simulation results. This explains the observation that water goes inside narrow carbon nanotubes in spite of the hydrophobic nature of the cavity. As the diameter of the tube increases, entropy and energy values approach those of bulk water.

Also Maiti *et al.* have shown that confined water molecules that are in a single-file arrangement inside narrow CNTs orientationally relax through angular jumps between two potential energy minima [61]. This bistable behavior is very different from the mechanism of jumps in the bulk, where thermally activated jumps make the system explore many locally stable minima. The angular jump of a water molecule in the bulk involves the breaking of a hydrogen bond with one of its neighbors and the formation of a hydrogen bond with a different neighbor. In contrast, the angular jump of a confined water molecule

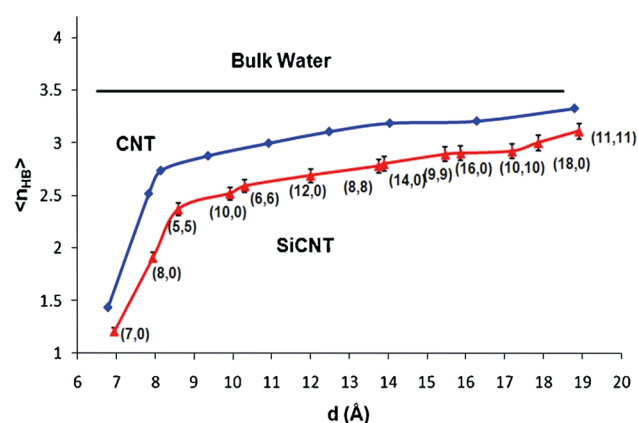


Fig. 2. Number of hydrogen bonds per water molecule, $\langle n_{HB} \rangle$, vs. the nanotube diameter, d . The blue, red and black lines correspond to CNT, SiCNT and bulk water. Reprinted with permission from ref. [64], © (2015), with permission from Elsevier.

corresponds to an interchange of the two hydrogen atoms that can form a hydrogen bond with the same neighbor.

Enhanced water flow through atomic smooth and hydrophobic CNTs has been demonstrated by theoretical calculations. For example, Holt *et al.* have reported water flow measurements through CNTs with diameters of less than 2 nm which serving as pores [62]. They have shown that the measured water flow exceeds the values calculated from continuum hydrodynamics models by more than three orders of magnitude and is comparable to flow rates extrapolated from MD simulations. Also pressure-driven water flow through CNTs with diameters ranging from 1.66 to 4.99 nm was examined by Thomas and McGaughey using MD simulation [63]. They have found that the flow rate enhancement, defined as the ratio of the observed flow rate to that predicted from the no-slip Hagen Poiseuille relation, is calculated for each CNT. The enhancement decreases with increasing CNT diameter and ranges from 433 to 47. Also the dynamics and structure of the confined water in single-walled silicon carbon nanotubes (SWSiCNTs) have been investigated by Taghavi *et al.* [64]. The water diffusion coefficients in SWSiCNTs were larger than those in SWCNTs and single-walled boron-nitride nanotubes (SWBNNTs). Furthermore, it was observed that water has a lower diffusion coefficient inside zigzag SWCNTs than armchair SWCNTs. In fact, the diffusion of water molecules inside SWSiCNTs is based on a ballistic motion mechanism. The difference between the diffusion coefficient in (6, 6) and (10, 0) SWSiCNTs could be the result of the orientation of water molecules inside SWSiCNTs. In fig. 2 the number of hydrogen bonds per water molecule, $\langle n_{HB} \rangle$, vs. the nanotube diameter, d , was illustrated. Figure 2 shows that $\langle n_{HB} \rangle$ inside SWSiCNTs is always lower than that of bulk water.

Pascal *et al.* have reported the entropy, enthalpy, and free energy extracted from MD simulations of water confined in CNTs from 0.8 to 2.7 nm diameters [65]. They have found for all sizes that water inside the CNTs is

more stable than in the bulk, but the nature of the favorable confinement of water changes dramatically with CNT diameter. Thus they showed that free energy under confinement is due primarily to the increased rotational and translational entropy for small CNTs but mainly increased translational entropy for larger CNTs, except in the case of the 1.1 and 1.2 nm CNTs where the rigid H-bonded water framework leads to favorable enthalpy. Thus the thermodynamics of water under confinement are intimately connected to the structure of water and its commensurability with the pore sizes. MD simulations have been performed under physiological conditions using nanotube segments of various diameters submerged in water. The results show that water molecules can exist inside the nanotube segments and that the water molecules inside the tubes tend to organize themselves into a highly hydrogen-bonded network, *i.e.* solid-like and wrapped around ice sheets. The disorder-to-order transition of these ice sheets can be achieved purely by tuning the size of the tubes [66].

2.2 Confinement within the graphene and its derivations

Other types of nano matrices have been analyzed extensively for confinement are graphene and its derivation [67, 68]. Since the discovery of graphene [69] and after many successful advances in manufacturing methodologies [70], there has been a growing interest in the study of the solid-water molecule intercalated into a bilayer graphene, the constraints of this interlayer conformation strongly affecting the adsorption sites and the orientation of the water molecule [71]. The characterization of the geometric and electronic structure of a nanoscale confined water within two parallel graphene sheets was reported by Song *et al.* [71]. They have shown that the O–H bonds of the water molecules become almost parallel to the bilayer; when the distance between the graphene bilayer is reduced to 4.5 Å, however, further reducing the distance to 4.0 Å induces an abnormal phenomenon characterized by several O–H bonds pointing to the graphene surface. Also, it has been shown that viscosity [72], permittivity [73], ion adsorption/solvation [74] differ significantly from their bulk values as well. Furthermore, these properties combined allow calculating interfacial capacitances and challenge continuum models, *e.g.* the double layer model.

In a related study, Mari *et al.* have reported the MD simulations of water at ambient and high temperature, under supercritical conditions onto a graphene slab 3.1 nm wide [75]. In this context, they compared all collected data within a broad range of densities and temperatures and then, investigated the relationship between the microscopic structure and dynamics of the system and the effect of hydrophobic and thermodynamic confinement. Some of the observations reported by the authors included structural weakening as a result of massive hydrogen bond breaking, a gradual rise of water self-diffusion coefficients, reduction of residence times and permittivity in selected regions, and the presence of spectral shifts due to changes in atomic and molecular vibrations. Eslami *et al.* have

also described the dynamics and structure of hydrogen bonds (HBs) in nanoconfined water between the parallel graphene surfaces [76]. The results indicated that the structure of HBs is strongly affected by layering of water molecules nearby the surfaces. Very close to the surfaces, the geometrical restrictions will result in the preferential orientation of the hydrogen atoms of water toward the surfaces, and therefore, scarify their HB network. This group also showed that in comparison with the corresponding bulk value, a reduction in the number of HBs per donor was observed in the layering of water molecules beside the surfaces. Generally, the confinement of water between hydrophilic surfaces leads to a distortion of the H-bond network, which can be expressed by a decrease in the value of the parameter ROH [77].

Deshmukh *et al.* have performed MD simulations to study the fluxional properties and atomic scale characterization of water molecules in the proximity of the graphene interface [78]. Based on the simulations, it was observed that the solvation dynamics, local orientation, and ordering of interfacial water molecules were strongly correlated to the graphene slit width. It was also reported that systematic trends in libration, stretching and bending bands were associated to hydrogen-bonding network and local ordering of water molecules. Strongly confined water molecules in comparison with the bulk water resulted in greater blue shifts in the O...O intermolecular stretching modes and smaller blue shifts in the intermolecular O...O...O bending mode of water molecules. This could be ascribed to the interfacial proximity effects leading to restricted transverse oscillations of the confined water. In another study, Chialvo *et al.* have studied via molecular dynamics the link between the strain-driven hydration free energy changes in the association procedure, including finite-size graphene surfaces, the combined effect of the surface strain and confinement and the resulting water-graphene interfacial tension on the dynamics and the thermodynamic response functions of confined water [79]. It was demonstrated that an in-plane biaxial tensile strain $\varepsilon = 10\%$ will result in a significant enhancement both in the water-graphene hydrophobicity with respect to that of the unstrained counterpart, and also in the confinement impact on the thermodynamic response functions and a deceleration of the dynamics of water over those of the corresponding bulk counterpart.

Recently, Zokaie and Foroutan employed MD simulations to compare the dynamical and structural properties of the water confined between two graphene sheets and between two Graphene Oxide (GO) sheets [80]. The results confirmed that under confinement conditions the dynamics and structure of water will change near the GO surfaces. The heterogeneous nature of the confined water was proved by different orientations of the water molecules to the GO sheets. It was observed that the isolation of water molecules in areas close to the GO surfaces, together with the formation of hydrogen bonds between the substituents of the GO and water molecules, will result in fewer hydrogen bonds between the water molecules with other water molecules around. It has been seen that in the middle region between two GO sheets, each water molecule

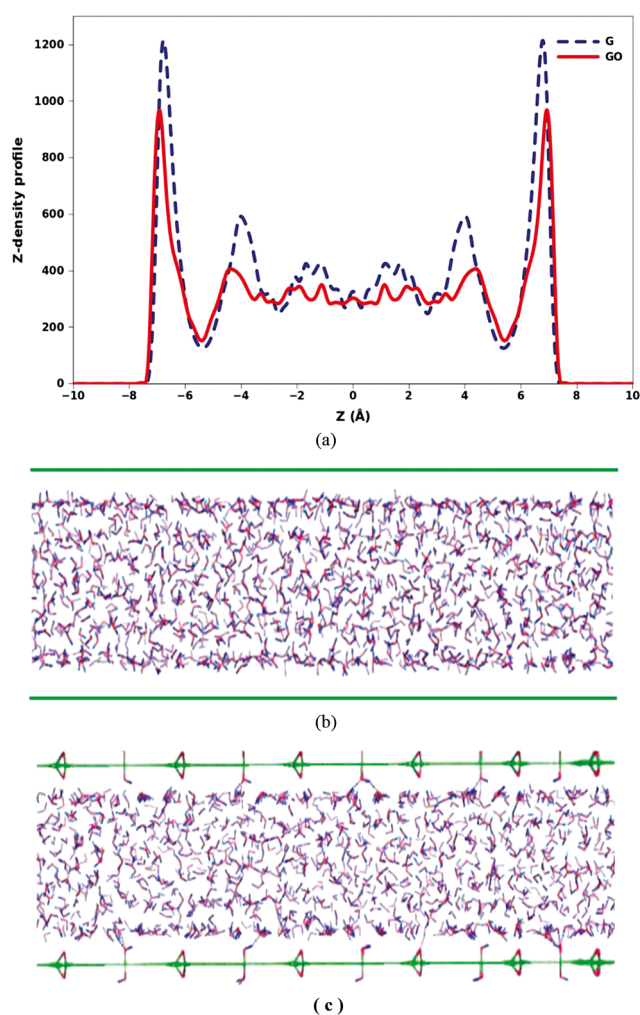


Fig. 3. (a) Z-density distribution of the oxygen atoms of water molecules confined between two graphene surfaces (dashed line) and two graphene oxide surfaces (solid line). Snapshot images of the water molecules confined between two graphene surfaces (b) and two graphene oxide surfaces (c) at the end of the simulation time. Green, red, and blue colors correspond to carbon, oxygen, and hydrogen atoms, respectively. Reprinted with permission from ref. [80], © (2015), with permission from Royal Society of Chemistry.

was surrounded by more water molecules, and as a consequence, there were much more hydrogen bonds in this region, in a way that it can be considered as a network structure of water.

Figure 3a presents the density profile of the oxygen atoms of water molecules confined between two surfaces of graphene (dashed line) and two surfaces of GO (solid line). In both cases, the density next to the surfaces is more than the one near the center. In the density profile three different bunches of water molecules can be seen. In the region between -2.5 \AA and 2.5 \AA , in the center to confinement surfaces of the GO, a straightforward line can be seen, and also the amount of density is in agreement with the bulk water density. At the distance of 2.5 \AA to 5.4 \AA (also at the distance of -2.5 \AA to -5.4 \AA) one peak

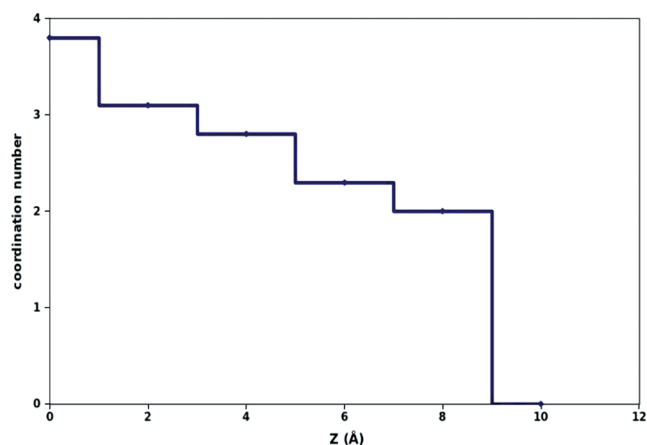


Fig. 4. Coordination number of water molecules as a function of distances between two graphene oxide sheets. Reprinted with permission from ref. [80], © (2015), with permission from Royal Society of Chemistry.

is observed in the midsection of both graphene and GO. The height of this peak in the graphene is more than that for the GO. Figures 3b and c show snapshot images of the water molecules confined between two graphene and GO surfaces, respectively at the end of 10 ns simulation time.

Figure 4 shows the coordination number at different distances from the confining surfaces of GO. Figure 4 shows that with the increase in the distances from confining surfaces, the coordination number increases, and in the central region this number is 3.8, that is more than other regions. This proves that in this midsection between the confining surfaces, there are more molecules around each water molecule.

Also, the liquid-solid phase transition temperature of water confined between two GO sheets was investigated using MD simulations by the same authors [81]. They have shown that due to the presence of functional groups of the GO sheets, at temperatures below the liquid-solid phase transition temperature, the water molecules near the confining sheets are not structured like ice and remained in the liquid form. The results also reveal the confinement effects on the melting and freezing rate of water molecules. The confining conditions delay the freezing process of the water molecules compared to the bulk water molecules. The liquid-solid phase transition temperature of water in the presence of GO sheets was calculated as 236 K, which was 34 K less than the temperature of the bulk water.

The phase behaviors and structures of highly confined water, amorphous ice, ice, and clathrate, in slit graphene nanopores have been studied by Zeng *et al.* [82]. In this report, six crystalline phases of the monolayer (ML) ice including one low-density, one mid-density, and four high-density ML ices were surveyed using MD simulations. Furthermore, an additional supporting evidence was provided to show the stabilities of the structures of the four high-density ML ices in the vacuum. The simulations show that both the disruption of the hydrogen bonding network in bulk water and compliance of the ice rule for low-density and high-density (quasi-two-dimensional) Q2D crystalline

structures are the results of the nanoscale confinement. In this regard, as a generic model system, highly confined water can be used for understanding a considerable diversity of Q2D materials science phenomena, including solid-solid, solid-amorphous, amorphous-amorphous and liquid-solid transitions in real time, and also the Ostwald staging during these transitions. The melting/freezing point of confined water between two graphene sheets were calculated from the direct coexistence of the solid-liquid interface by Foroutan *et al.* [83]. The phase transition temperature of the confined ice-water mixture was calculated as 240 K that was 29 K less than the non-confined ice-water system. They have shown that water molecules located in the layer near each graphene sheet with the thickness of 2 nm had a different behavior from other water molecules located in other layers. The results demonstrated that water molecules in the vicinity of graphene sheets had more mean square displacements than those in the middle layers. Also, it has been found that freezing and melting of water in nanometer-sized pores occurs at temperatures much lower than in bulk [84], the melting point of water, which decreases when the liquid is confined inside materials with pore diameters smaller than 10 nm follows the so-called Gibbs-Thomson law [85].

2.3 Confinement within other types of nano matrices

Layfield *et al.* used MD simulations to study the dynamic and structural characteristics of the confined water between alkanethiol hydrophobic self-assembled monolayers (SAMs) [86]. It was demonstrated that the surface has no significant effect on water-film depths of about 1 nm for the studied structural properties. However, beyond 1 nm, the SAMs clearly induce enhancement of water motion. It was also observed that the improved lateral diffusion coefficients persist into deeper areas of the water film than the other measure of the hydrophobic effect.

Figure 5 shows the density of water confined between two $7.5 \text{ nm} \times 6.5 \text{ nm}$ SAM plates separated by 5.0 nm. The depletion layer formed between the surface and the water film creates a peak in the density of the water closest to the surface with a value well above 1 g cm^{-3} . This first peak is consequently followed by a well in the density of water below the bulk density value. This density layering continues to propagate into the water film, but as fig. 5 shows, it vanishes less than 1 nm into the thin film.

In another study, Hu *et al.* considered the distribution of saline water in organic and inorganic pores as a function of pore morphology and pore size [87]. They proved that the distribution of water and ions in organic and inorganic pores as well as water entrapment mechanism are greatly dependent on the pore width and pore surface mineralogy.

Calcium silicate hydrate (C-S-H) is a kind of mesoporous amorphous material with the confined water in the gel pores, which provides a suitable medium for exploring the dynamics, structure and mechanical properties of the ultraconfined interlayer water molecules. Hou *et al.* have prepared the C-S-H gels with different compositions

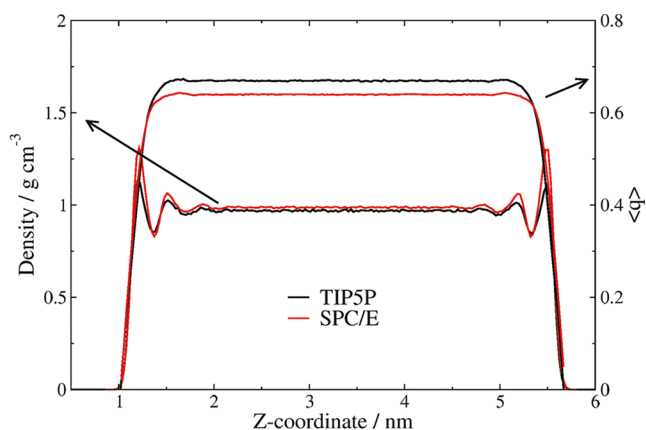


Fig. 5. Density profiles and average tetrahedrality for water molecules confined between two $7.5 \text{ nm} \times 6.5 \text{ nm}$ SAM surfaces separated by 5.0 nm at 300 K. The left y -axis is for the density and the right y -axis is for the tetrahedrality. Reprinted with permission from ref. [86], © (2015), with permission from American Chemical Society.

which were expressed in terms of the Ca/Si ratio and MD simulation was used for their characterization [88]. It was reported that increasing the Ca/Si ratio will result in the transformation of the molecular structure of silicate skeleton from an ordered to an amorphous structure. As the representative of the substrate, the calcium silicate skeleton has a considerable effect on reactivity, H-bonds network, the adsorption capability and mobile ability of the interlayer water molecules. On the one hand, it was observed that the silicate chains depolymerize to enhance the load resistance by acting in a skeletal role in the layered structure. On the other hand, water molecules dissociate into hydroxyls by attacking the Si-O and Ca-O bonds.

Figure 6 shows that the diffusion rate of atoms is ranked in the following order: $O_s > O_h > O_w$. A large MSD value at time t indicates that the atoms diffuse rapidly and are displaced far away from the original position. Different MSD curves characterize the chemical bonding and the physically associated water molecules.

The dynamics of the confined water in proteins are completely different from the dynamics of water in the bulk systems. Toward this end, Gnanasekaran *et al.* used MD simulations to study the dynamics of water at the interface of the two globules of the homodimeric hemoglobin from *Scapharca inaequivalvis* (HbI), with particular attention to the rotational anisotropy of the interfacial water molecules and water-protein hydrogen bond lifetimes [89]. They reported that the relaxation times of tens to thousands of picoseconds and stretched exponentials with exponents from 0.1 to 0.6 could be used to describe the relaxation of the waters at the interface of both oxy- and deoxy-HbI, including a cluster of 11 and 17 interfacial waters, respectively. It was observed that there is a slower rotational relaxation and hydrogen bond rearrangement for the interfacial water molecules of oxy-HbI than those of deoxy-HbI. This phenomenon is based on an allosteric transition from unliganded to liganded conformers including the expul-

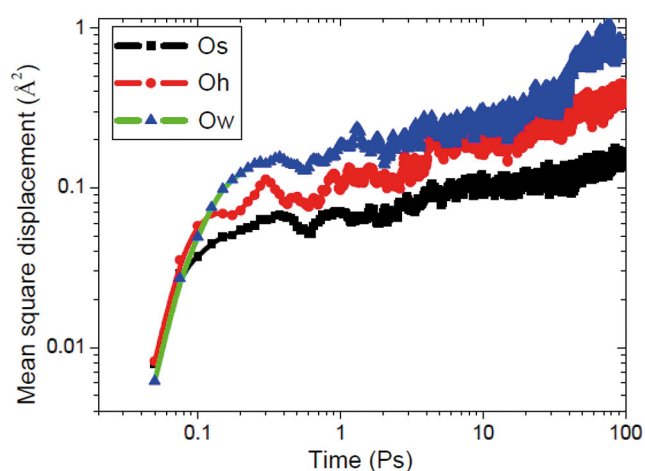


Fig. 6. Mean square displacement of Os, Ow and Oh atoms; Ow represents the oxygen atom in the water molecule; Oh is O in the Ca-OH and Si-OH groups; Os is O in the silicate chains without hydroxylation. Reprinted with permission from ref. [88], © (2015), with permission from American Chemical Society.

sion of some water molecules from the interface. Another investigation on both the dynamical and structural properties of water confined in a highly cross-linked polyamide reverse-osmosis membrane was reported by Ding *et al.* using MD simulations [90], in the presence of a main HB network formed by about 90% of the water molecules within the polyamide membrane. In addition, the authors showed that long range correlation is the result of the presence of some small water clusters into the matrix. MD simulations also indicated that a non-negligible amount of confined water molecules exhibits rather large rotational jumps (as in bulk phase) inside the membrane which is considered to be a prerequisite for HB formation. The results showed that in the central part of the membrane the translational diffusion coefficient of confined water was reduced by an order of magnitude in comparison with the bulk phase.

It is however well known that hydrophilic surfaces have substantially different properties [91]. Interestingly, Choudhury has investigated the effect of the degree of hydrophilicity or hydrophobicity of the plates on the dynamics of confined water between the two plates using MD simulations of water in and around a pair of plates immersed in water [92]. It was observed that by varying plate-water dispersion interaction, the nature of the plate changed from hydrophobic to hydrophilic and vice versa. Furthermore, by increasing the hydrophilicity of the plates, a monotonically decreasing trend of the diffusivity was achieved. The same monotonic trend was also pursued for orientation dynamics of the confined water. In spite of the fact that increasing of plate-water dispersion interaction in the hydrophobic region related to the smaller plate-water attraction almost has no effect on orientation time constant, it has considerable changes in the hydrophilic region corresponding to larger plate-water dispersion interactions. It has been reported that the diffusion coefficient

of confined water decreases by 3 to 4 orders of magnitude when it transforms into a frozen state [93].

3 Nanoconfinement of ionic liquids

In this section, the structure of confined ionic liquids (IL) in narrow and large confinements is analyzed, respectively. We discuss structure of IL when confined in a carbon nanotube followed by graphene and finally investigate a few types of nano matrices.

In the last two or three decades the emphasis on the concept of “green chemistry” has become one of the most important topics among scientists in related areas [94]. Worldwide demand for environmentally friendly green chemistry resulted in the development of novel approaches in synthesis, extraction, catalysis and separation, as well as electrolytic processes. IL, possessing many novel properties, is the most competitive candidate that caters to all trades and professions. Properties such as non-flammability [95], high ionic conductivity [96], electrochemical and thermal stability of ILs [97] make them ideal electrolytes in electrochemical devices like in batteries [98], capacitors [99], fuel cells [100], photovoltaics [101], actuators [102] and electrochemical sensors [103]. In addition, ILs have been widely used in electrodeposition, electrosynthesis, electrocatalysis, electrochemical, lubricants, plasticizers, solvent, lithium batteries, solvents to manufacture nanomaterials, extraction, gas absorption agents [104], and so forth [105].

One of the most important issues for the extensive use of ILs is decreasing their melting point (m.p.). Up to now, the structure of ILs and their phase behavior have been widely studied [106] and a many efforts including adding other ILs or organic compounds, changing the structure of the component ions [107,108] and confining the ILs into the fine pores have been made to lower the m.p. of the ILs [109].

Over the past few decades, ILs have experienced exponential growth in research activity [110]. Task-specific ILs have been used as alternatively supported tools [111], scavengers [112], catalysts [113] and reagents [114] as well in combinatorial chemistry (instead of polymers) due to their unique properties. It is well known that ILs and other fluids when confined in nano-sized cavities, display anomalous properties, which are illustrated by melting point depression, boiling point elevation, changes in hydrogen bonding of the fluid, variation in the secondary structure in proteins, etc. [115] Expanding upon the ideas of confinement of water and other fluids, successful attempts have been made to confine ILs in microemulsions [116], micelles [117], controlled pore glasses [118], silica gels [119] and kaolinite [120]. The first study of IL confined by a microemulsion was reported by Gao *et al.* [121] employing the IL 1-butyl-3-methyl-imidazolium tetrafluoroborate ([bmim][BF₄]). They prepared [bmim][BF₄]/Triton X-100/cyclohexane microemulsions and characterised them by various experimental techniques, and they found that the size of the polar IL increases, akin to conventional microemulsions with water polar domains.

3.1 Confinement within carbon nanotubes

Singh *et al.* have performed MD simulations to investigate the dynamical and structural properties of the IL [BMIM⁺][PF₆⁻] confined inside MWCNTs with inner diameters ranging from 2.0 to 3.7 nm [122]. The results revealed that the pore loading and the diameter of the MWCNT have a significant effect on both the dynamical and structural properties of the confined IL. A significant layering was observed with respect to the structural properties in the mass density profiles of the anions and cations along the radial direction. The cations close to the pore walls were aligned with their imidazolium ring parallel to the surface. In both the axial and the radial directions, regions of high and low density were observed upon reduction in the pore loading. About the dynamics, the confined cations move faster than the anions, in comparison with the bulk systems, but the dynamics in confinement are much slower than in the bulk. Before reaching the Fickian (diffusive) regime, the confined ions will remain in the “cage regime” for a long time. The results of this study suggested that the cations move faster in the center of the pore than close to the pore walls. The anions also show a similar trend, although the differences in dynamics are not as obvious as those observed for the layers of cations.

The melting procedure of the IL 1-butyl-3-methylimidazolium hexafluorophosphate ([bmim][PF₆]) crystals confined in CNT have been investigated in detail by Dou *et al.* using MD simulations [123]. It was observed that a “shell-chain” structure was formed within the nanopore by means of the confined ions. The results revealed that at low temperature, this “shell-chain” structure had long-range crystalline order and began to melt at about 500 K, which well fit with experimental observations of ILs in CNTs. The potential energy profile of the confined ions has also confirmed this melting process. The potential energy of cations and anions inside the nanopore *versus* temperature combined with typical snapshots are shown in fig. 7.

The ions inside the nanopores were approximately frozen around their positions below 500 K. As the temperature increased above 500 K, for each confined anion the average number of hydrogen bonds began to decline in a linear manner. Then, a dramatic change in the packing arrangement of the confined ions was observed as the result of this decline, followed by a steep rise in the ionic diffusivity. Melting points and the thermal decomposition temperature of several ILs have been reported to increase by more than 200 °C when confined inside MWCNTs [124, 125].

In a similar study, Foroutan and Balazadeh have performed MD simulations to determine the strong effects of confinement in a (20,20) CNT on the behavior of a mixture of 1-n-propyl-4-amino-1,2,4-triazolium bromide ([part][Br]) IL and water [126]. The effects of water mole fraction on the dynamical and structural properties of both IL/water mixture and confined IL/water mixture were investigated. They found that the highest interaction energy value was observed in pure IL systems and pure water in the case of confined IL/water mixtures. Finally,

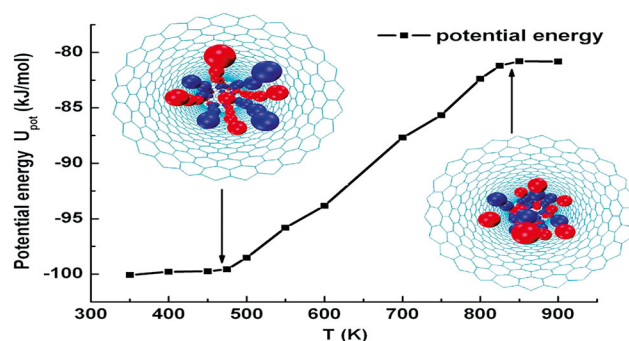


Fig. 7. The temperature dependence of confined-ions potential energy. The potential energy consists of cation-cation, cation-anion, and anion-anion intermolecular interactions and cation-walls and anion-walls interactions. The insets show the radial snapshots of the encapsulated ILs in nanopores before melting and after being molten entirely. Red and blue balls represent center-of-mass locations of bmim^+ and PF_6^- , respectively, Reprinted with permission from ref. [123], © (2015), with permission from American Chemical Society.

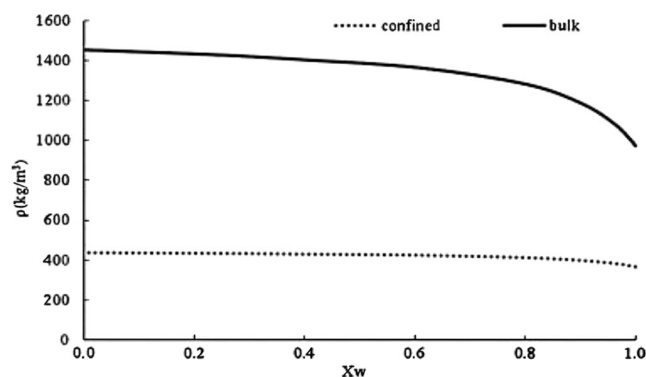


Fig. 8. Density profile for the confined water/[part][Br] mixtures (dash line) and their bulk mixtures (solid line). Reprinted with permission from ref. [126], © (2015), with permission from Elsevier.

the authors found that the presence of CNT has two effects including the tendency of cations to orient their rings mainly parallel to the CNT surface and also a stronger spatial correlation between IL molecules and water. The density profile of the water/[part][Br] mixtures confined inside (20,20) SWCNT and their bulk mixtures for all water mole fractions are shown in fig. 8.

As fig. 8 shows, the density of the bulk mixture and the confined mixture decrease with increasing water mole fractions. Akbarzadeh *et al.* have performed MD simulations to study the thermodynamics, structure, and dynamical behavior of 1-ethyl-3-methylimidazolium hexafluorophosphate [emim][PF] during the melting process inside CNTs with different radii [127]. They found that the layering occurs for the IL inside the zigzag and arm-chair CNTs with the local density maximums close to the CNT walls. The sharp peaks are also observed at low temperature. However, as the temperature increases, the peaks related to the layer structure near the CNT wall

become broader and less intense. They have shown that the average number of hydrogen bonds decreases as the temperature increases. The internal energy also increases slightly with increasing temperature, followed by a dramatic jump.

3.2 Confinement within graphene

Méndez-Morales *et al.* [128] analyzed the structure of the well-known formation of layers on liquids under confinement with the aid of MD simulations of mixtures of 1-butyl-3-methylimidazolium tetrafluoroborate [BMIM][BF₄] with lithium tetrafluoroborate LiBF₄ and potassium tetrafluoroborate KBF₄ between two parallel charged and uncharged graphene walls. The analysis showed the formation of a layered structure with ion densities higher than in the bulk. Furthermore, since the layers in the neutral surface are composed of both ionic species of IL, as the electrode potential increases, the structure will change to alternating cationic and anionic layers leading to an overcompensation of the charge in the previous layer. It was revealed that only for the highest amount of salt, potassium and lithium ions will be adsorbed on the negative surface. The negative graphene surface for both potassium and lithium cations is up to 0.28 nm and 0.21 nm, respectively. The closer distances to the negative electrode than the first cationic layer implies that a considerable amount of salt must be added to the IL for the adsorption of lithium/potassium cations on the graphene wall, which has a paramount importance for redox processes. This behaviour can be clearly observed in fig. 9.

Singh *et al.* have studied the dynamics and structure of the IL [EMIM⁺][TFMSI⁻] inside a rutile (110) slit nanopore using classical MD simulations [129]. The results were compared with those obtained from another study for the same IL inside a slit graphitic nanopore of the same width [130]. The results suggested that the strength of the interactions between the IL and the pore walls has a considerable effect on the dynamics and structure of the confined IL. For an IL inside a rutile pore the layering effects were more prominent in comparison with an IL inside a graphitic pore. A liquid structure was observed for the ions near the rutile pore walls which was noticeably different from that of the bulk IL; on the contrary, near graphitic pore walls the same ions had a liquid structure similar to that of the bulk IL. Multiple orientations of anions and cations near the rutile walls were in contrast with the parallel orientations uniformly observed for the same ions near graphitic walls. It was reported that the dynamics of the IL are significantly slower inside a slit rutile pore than those inside a slit graphitic pore. Furthermore, the dynamics of the ions near the rutile walls were an order of magnitude slower than ions near graphitic walls.

In another investigation, classical MD simulations were performed by Rajput *et al.* to study the dynamics and structure of the IL [emim⁺][NTf₂⁻] inside a realistic model of a coconut shell activated carbon (CSAC) and a slit graphitic nanopore [131]. Semi-graphitic carbon sheets in the CSAC model material have various shapes and sizes,

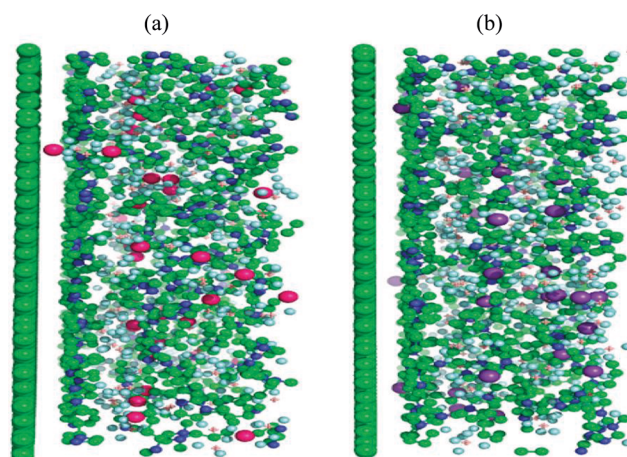


Fig. 9. Snapshots of the structural organization of the ions near negatively charged graphene walls from simulations of [BMIM][BF₄] doped with a 25% LiBF₄ (a) and 25% KBF₄ (b). The relative size of lithium (dark pink) and potassium (violet) atoms has been exaggerated for the purpose of clarity. Colour coding for the rest of the atoms is as follows: green carbon; dark blue nitrogen; light blue fluorine; and light pink boron. Hydrogen atoms have been removed for the purpose of clarity. Reprinted with permission from ref. [128], © (2015), with permission from Royal Society of Chemistry.

which develop irregular, connected pores with rectangular shape. In total, the ions inside the CSAC model material like for the IL inside slit pores, form layers parallel to the walls; although, the complex pore geometry of the CSAC model materials and the distribution of pore sizes result in the orientation of the ions and the density profiles to be completely different from the uniform behavior of these properties in the IL inside slit pores. Another reason that makes confinement effects weaker than in slit pores with the same size is the existence of interconnected pores along with a distribution of sizes in the CSAC model materials. As a result, a liquid structure similar to that of the bulk IL can be seen for the ions inside CSAC model materials and also faster dynamics than those of IL slit pores of the same size. As observed for the IL inside slit pores, the movement of the ions near the pore walls of the CSAC model material is slower than the ions farther away from the walls. However, variations of pore size with position within the CSAC model material and the complex pore geometry result in significant spatial heterogeneities of the dynamics of the confined IL and its departure from the regular uniform behavior observed in slit nanopores. Finally, it was concluded that the dynamics and structure of confined ILs inside porous materials with heterogeneities in pore shape, pore interconnectivity and pore size can be significantly different from the properties of confined ILs inside ideal pores with simple geometries. Figure 10 shows front views of (a) CSAC model, average pore size $H = 0.75$ nm, and (b) slit graphitic pore, size $H = 0.75$ nm (bottom panels).

Similarly, MD simulations were applied by Rajput *et al.* to study the dynamics and structure of the confined IL

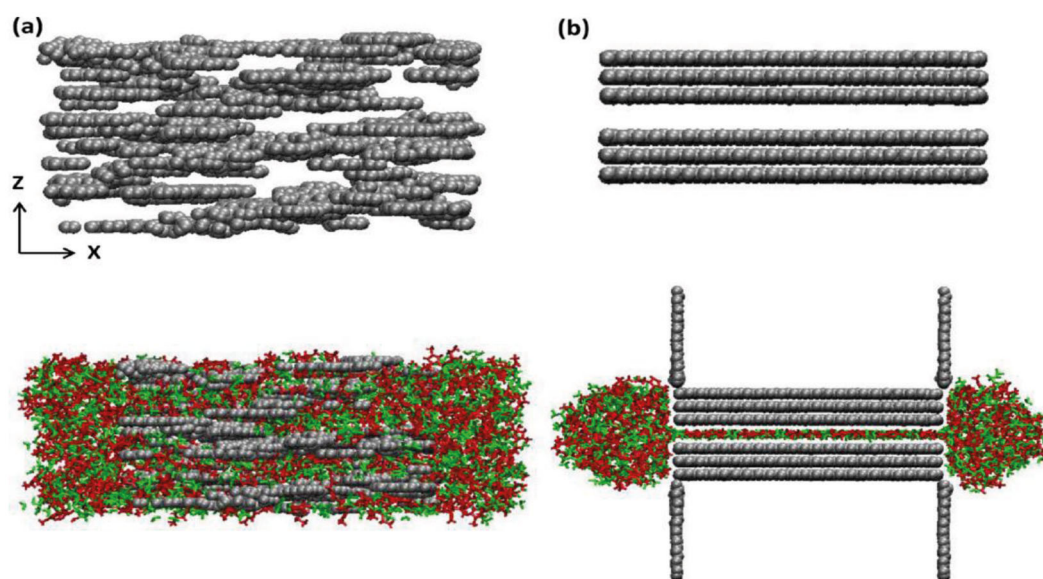


Fig. 10. Top panels: Front views of (a) CSAC model, average pore size $H = 0.75$ nm, and (b) slit graphitic pore, size $H = 0.75$ nm. Bottom panels: Representative simulation snapshots of the model systems studied, $H = 0.75$ nm and $T = 333$ K. Carbon atoms in the walls are depicted in gray; cations and anions are depicted in red and green. Reprinted with permission from ref. [131], © (2015), with permission from American Chemical Society.

[emim⁺][NTf₂⁻] inside a slit graphitic nanopore of width $H = 5.2$ nm and the pore walls with different densities of electrical charges [132]. The dynamics and the structure of the confined IL were strongly affected by the density of electrical charges, especially in those ionic layers near the electrically charged walls. By increasing the electrical charges in the pore walls, the local density of counterions increased together with important changes in the liquid structure of the ions, particularly in the layers close to the pore walls. Another effect of enhancement of electrical charges in the pore walls was inducing important changes in the dynamics of the confined ions.

The basic mechanisms of the formation of the interfacial layer at the neutral graphite monolayer (graphene)–IL (1,3-dimethylimidazolium chloride, [dmim][Cl]) interface have been successfully studied by Fedorov and Lynden-Bell using fully atomistic MD simulations [133]. In this regard, a significant enrichment of IL cations at the surface layer was observed. The attraction of Cl⁻ anions by this cationic layer leads to the formation of some distinct IL layers at the surface. The preferential adsorption of the IL cations at the graphene surface results in a strong asymmetry in cationic/anionic probe interactions with the graphene wall. The high density of IL cations at the interface causes an additional high-energy barrier for the cationic probe to come to the wall in comparison with the anionic probe. Using atomistic MD simulations, Wu *et al.* [134] have shown that confinement can result in an unusual behavior in the properties of ILs. Kohanoff *et al.* [135] simulated the molten salt 1,3-dimethylimidazolium chloride confined between two flat parallel walls and showed a structure of layers parallel to the walls. Recently, Kim *et al.* [136] studied the superca-

pacitors consisting of two single-sheet graphene electrodes and found that, in contrast to the emim, anion was more efficient in shielding electrode charges. Foroutan and Balazadeh have investigated the structure, morphology, behavior, and dynamical properties of pure IL ([emim][BF₄]) confined between two flat and parallel graphene sheets at different interwall distances, H [137]. For this purpose, various interwall distances including 10, 14, 16, 20, 23, and 28 Å were studied by MD simulations at seven temperatures ranging from 278 to 308 K. It was found that the orientation and distribution of anions and cations on the graphene sheets depended on the interwall distances. In this context, a dense monolayer of the cations and anions was formed between two graphene sheets at the shortest H . By increasing H , the number of layers increased. Furthermore, by increasing temperature and H , diffusion coefficients of the anions and cations increased. It was revealed by orientation functions that most of the cations had parallel orientations to the graphene sheets. Akbarzadeh *et al.* have presented MD simulations on the IL [emim][PF₆] confined between the graphite sheets with different distances ranging from 1 to 5 nm [138]. They showed a significant layering occurs at the IL-graphite interface which indicates a strong interaction between the IL and the graphite sheets. They have found that the average number of the hydrogen bonds increased as the pore size decreased. The average number of the H -bonds also increases as the pore loading increases. They showed that the self-diffusion coefficient of both cations and anions increases with increase in pore size. Also, the self-diffusion of the confined ions decreases with increasing the pore loading.

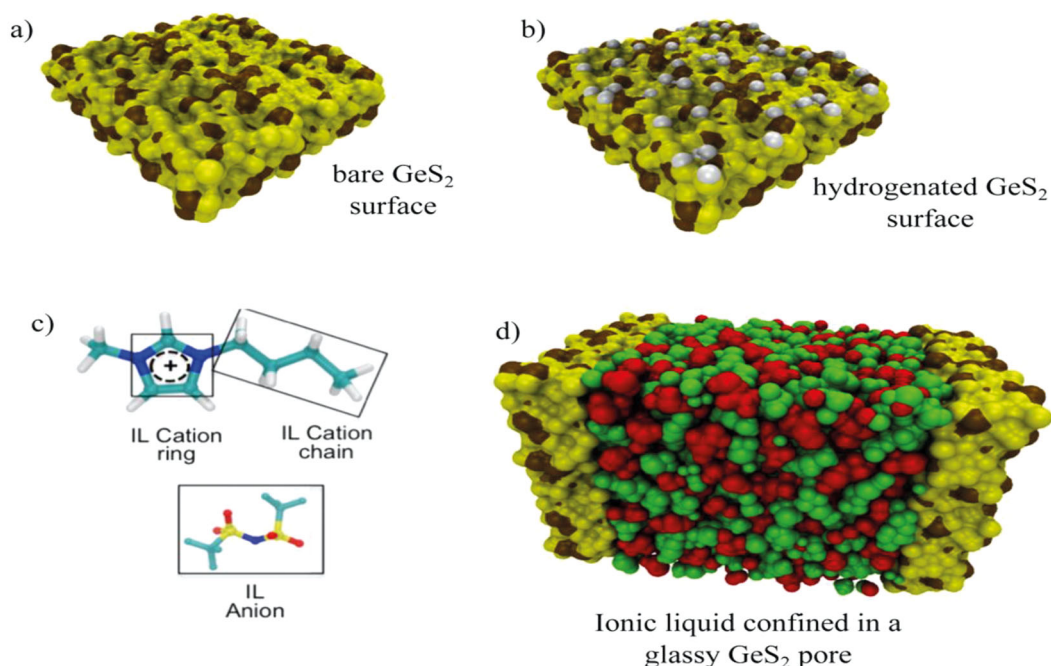


Fig. 11. Atomic surface models of bare (a) and hydrogenated (b) GeS_2 . The yellow, ochre, and white balls are the S, Ge, and H atoms of the surfaces, respectively. (c) Chemical structure of the IL: 1-butyl-3-methylimidazolium (cation) and bis(tris(trifluoromethyl)sulfonyl)-imide (anion) where different fragments of the IL are highlighted. The color code is (cation) N dark blue; C light blue; H white; and (anion) S yellow; O red; F light blue; N dark blue. (d) Typical molecular configuration for the IL confined in a chalcogenide pore of a width $H = 4.8$ nm at $T = 300$ K. The red and green spheres are the atoms of the IL anion and cation, respectively, Reprinted with permission from ref. [141], © (2015), with permission from American Chemical Society.

3.3 Confinement within other types of nano matrices

In a study by Gupta *et al.* it was observed that the glass transition temperature of the IL 1-ethyl-3-methylimidazolium ethyl sulfate $[\text{EMIM}][\text{EtSO}_4]$ immobilized in silica matrix was $\sim 20^\circ\text{C}$ higher than the bulk IL [139]. Upon confinement, the thermal stability of $[\text{EMIM}][\text{EtSO}_4]$ also increased. The interactions between the organic cation $[\text{EMIM}]^+$ and anion $[\text{EtSO}_4]^-$ of the IL and the inorganic SiO_2 pore wall surface explain these changes. MD simulations were also used by Ori and coworkers to study the structure and dynamics of a confined IL in hydroxylated amorphous silica nanopores at ambient pressure and temperature [140]. The results showed that both the dynamics and structure of the confined IL can be explained as the sum of a bulk-like contribution arising from the ions located in the pore center and a surface contribution resulted from the ions in contact with the surface. It can be concluded that the surface-to-volume ratio of the host porous material is the most important factor to determine the properties of the confined IL. However, the ionic conductivity that is a collective dynamical property of the confined IL, is similar to the bulk. The same group also employed MD simulations to study the dynamical and structural properties of a typical confined IL in a realistic molecular model of amorphous chalcogenide having different surface chemistries and pore sizes [141]. It was found that both self-dynamics and the

structure of the confined phase are related to the surface-to-volume ratio of the host confining material. Finally, the collective dynamical properties, *e.g.* the ionic conductivity, remain approximately insensitive to surface chemistry and pore size and will be similar to their bulk counterpart. Figure 11 shows the models of bare and hydrogenated GeS_2 surfaces and the IL.

In another study, Canova *et al.* used MD simulations to study the shear dynamics and structure of two confined ILs between two hydroxylated silica surfaces having the same cation 1-butyl-3-methyl-imidazolium (BMIM), paired with tetrafluoroborate $[\text{BF}_4^-]$ and bis(trifluoromethanesulfonyl)amide $[\text{NTF}_2^-]$ anions [142]. The simulated dynamics explained the effect of the layered structure of nanoconfined liquids on dynamical properties at the molecular level and also the relationship between the shape of IL molecules and their layering structure at hydroxylated silica surfaces. In the case of shearing of $[\text{BMIM}][\text{NTF}_2]$, larger molecular oscillations in the inner layers are needed to allow the system to stabilise and an irregular dynamics are obtained. In contrast, the alternating charged layers in $[\text{BMIM}][\text{BF}_4]$ result in the stabilization of the system via smaller fluctuations, and the layers shear on top of each other in a fashion of laminar.

The calculation of the excess enthalpies of some imidazolium-based ILs having various anions and water has been carried out by Ficke and Brennecke [143]. Re-

cently, the mutual solubility of some imidazolium-based ILs and water has been widely discussed [144–146]. Feng and Voth have studied how the [bmim][BF₄] IL behavior is affected by the alkyl side chain length and anion [147]. It was found that alkyl chain length plays a crucial role in the aggregation behavior of the cations. In fact, a stronger aggregation of the cations and slower diffusion of the anions was observed by the increase of the alkyl chain length. More recently, Varela *et al.* studied water/1-alkyl-3-methylimidazolium IL mixtures using MD simulations and the formation of water cluster were confirmed in these mixtures [148].

Singh *et al.* [149] have demonstrated that phase transition temperatures and thermal stability of [emim][BF₄] on confinement in the nanopores of silica matrix changed significantly from the bulk IL. The DFT calculation indicated that the interaction of the IL with the surface resulted in changes in the vibrational bands. Singh *et al.* [150] have considered the crystallization kinetics of pure IL [emim][BF₄] and IL confined in mesopores silica matrices. They found a significant influence of confinement on the crystallization rate and also crystallization dimensionality of IL.

In another work, 1-ethyl-3-methylimidazolium tetrafluoroborate [emim][BF₄] confined in a silica matrix (ionogel) was synthesized by the same research group at different gelation temperatures and it was observed that the gelation rate was lower at lower temperatures [151].

4 Conclusions

The different MD simulation approaches highlighted throughout this review have illustrated how nanoconfinement of water and ILs can evidence physical behaviors not observed in their bulk analogs. In water-confined system, the results showed that the microscopic static structure of water inside nano-sized cavities has been the identification of an alteration in the hydrogen bonding network of water in nanoscale confinement. The obtained results confirm the heterogeneous structure of confined water molecules and water molecules have different orientations at various distances from the confining surfaces. Water molecules next to the confining surfaces are more affected by the surfaces and owing to the formation of the hydrogen bond between water molecules and functional groups of confining surfaces in this region, the number of hydrogen bonds between water molecules decreases. In the case of ILs in nanoscale confinement, by comparing several recent MD simulations, some general features of ion arrangements and dynamics in confined geometries have been identified. The results indicated that a layering behavior of the anion and cation was observed for the IL [emim][BF₄] at different distances between two graphene sheets. Also, cations and anions tended to form aggregations around each other. The diffusion values of the cations and anions increased as the temperature and distances between the two graphene sheets increased.

Author contribution statement

All authors contributed equally to the paper.

References

1. P. Das, *Nanoscale* **4**, 2931 (2012).
2. L.B. Krott, M.C. Barbosa, *Phys. Rev. E* **89**, 012110 (2014).
3. A.C. Fogarty, F.X. Coudert, A. Boutin, D. Laage, *ChemPhysChem* **15**, 521 (2014).
4. O. Ciftja, *Int. Nano Lett.* **2**, 36 (2012).
5. M.P. Singh, R.K. Singh, S. Chandra, *Prog. Mater. Sci.* **64**, 73 (2014).
6. A. Pajzderska, P. Bilski, J. Wąsicki, *J. Chem. Phys.* **142**, 084505 (2015).
7. B. Karimi, A. Zamani, F. Mansouri, *RSC Adv.* **4**, 57639 (2014).
8. K. Arya, B. Prabhakar, *Green Chem.* **15**, 2885 (2013).
9. N. Naguib, H. Ye, Y. Gogotsi, A.G. Yazicioglu, C.M. Megaridis, M. Yoshimura, *Nano Lett.* **4**, 2237 (2004).
10. C.Y. Won, N. Aluru, *J. Phys. Chem. C* **112**, 1812 (2008).
11. D. Blach, M. Pessêgo, J.J. Silber, N.M. Correa, L. García-Río, R.D. Falcone, *Langmuir* **30**, 12130 (2014).
12. D.A. Kunz, M.J. Leitl, L. Schade, J. Schmid, B. Bojer, U.T. Schwarz, G.A. Ozin, H. Yersin, *J. Breu, Small* **11**, 792 (2015).
13. M. Pagliai, G. Cardini, R. Cammi, *J. Phys. Chem. A* **118**, 5098 (2014).
14. G. Cicero, J.C. Grossman, E. Schwegler, F. Gygi, G. Galli, *J. Am. Chem. Soc.* **130**, 1871 (2008).
15. M. Ghosh, L. Pradiptanti, V. Rai, D.K. Satapathy, P. Vayalamkuzhi, M. Jaiswal, *Appl. Phys. Lett.* **106**, 241902 (2015).
16. B. Rossi, V. Venuti, A. Mele, C. Punta, L. Melone, V. Crupi, D. Majolino, F. Trotta, F. D'Amico, A. Gessini, *J. Chem. Phys.* **142**, 014901 (2015).
17. H. Ōkawa, M. Sadakiyo, K. Otsubo, K. Yoneda, T. Yamada, M. Ohba, H. Kitagawa, *Inorg. Chem.* **54**, 8529 (2015).
18. R. Renou, A. Szymczyk, G. Maurin, A. Ghoufi, *Mol. Simul.* **41**, 483 (2015).
19. A.A. Milischuk, B.M. Ladanyi, *J. Chem. Phys.* **135**, 174709 (2011).
20. Q. Li, J. Song, F. Besenbacher, M. Dong, *Acc. Chem. Res.* **48**, 119 (2014).
21. G. Hummer, J.C. Rasaiah, J.P. Noworyta, *Nature* **414**, 188 (2001).
22. G. Zuo, R. Shen, W. Guo, *Nano Lett.* **11**, 5297 (2011).
23. X. Qin, Q. Yuan, Y. Zhao, S. Xie, Z. Liu, *Nano Lett.* **11**, 2173 (2011).
24. J.P. Hallett, T. Welton, *Chem. Rev.* **111**, 3508 (2011).
25. S.M. Fatemi, M. Foroutan, *J. Nanostruct. Chem.* **5**, 243 (2015).
26. T.Y. Kim, H.W. Lee, M. Stoller, D.R. Dreyer, C.W. Bielawski, R.S. Ruoff, K.S. Suh, *ACS Nano* **5**, 436 (2010).
27. G. Appetecchi, G.-T. Kim, M. Montanino, M. Carewska, R. Marcilla, D. Mecerreyes, I. De Meazza, *J. Power Sources* **195**, 3668 (2010).
28. G.P. Lau, H.N. Tsao, S.M. Zakeeruddin, M. Grätzel, P.J. Dyson, *ACS Appl. Mater. Interfaces* **6**, 13571 (2014).

29. S. Perkin, Phys. Chem. Chem. Phys. **14**, 5052 (2012).
30. E.D. Hazelbaker, R. Guillet-Nicolas, M. Thommes, F. Kleitz, S. Vasenkov, Microporous Mesoporous Mater. **206**, 177 (2015).
31. H. Abe, T. Takekiyo, M. Shigemi, Y. Yoshimura, S. Tsuge, T. Hanasaki, K. Ohishi, S. Takata, J.-i. Suzuki, J. Phys. Chem. Lett. **5**, 1175 (2014).
32. H.-P. Steinrück, Phys. Chem. Chem. Phys. **14**, 5010 (2012).
33. C. Merlet, M. Salanne, B. Rotenberg, J. Phys. Chem. C **116**, 7687 (2012).
34. Y. Zhu, J. Zhou, X. Lu, X. Guo, L. Lu, Microfluid. Nanofluid. **15**, 191 (2013).
35. M. Foroutan, S. Khoei, *Computational Nanotechnology: Modeling and Applications with MATLAB®*, edited by S.M. Musa (CRC Press, Boca Raton, 2011) p. 251.
36. M. Foroutan, S.M. Fatemi, *Encyclopedia of Nanoscience and Nanotechnology*, edited by H.S. Nalwa (American Scientific Publishers, Valencia, CA, 2017).
37. M. Tarek, D. Tobias, Phys. Rev. Lett. **88**, 138101 (2002).
38. M.A. Henderson, Surf. Sci. Rep. **46**, 1 (2002).
39. H. Kim, M.D. Annable, P.S.C. Rao, Environ. Sci. Technol. **35**, 4457 (2001).
40. Y. Rudich, I. Benjamin, R. Naaman, E. Thomas, S. Trakhtenberg, R. Ussyshkin, J. Phys. Chem. A **104**, 5238 (2000).
41. V. Buch, J.P. Devlin, *Water in Confining Geometries* (Springer Science & Business Media, 2013).
42. L.B. Da Silva, J. Nanostruct. Chem. **4**, 1 (2014).
43. S.M. Fatemi, M. Foroutan, Adv. Sci. Eng. Med. **6**, 583 (2014).
44. S.M. Fatemi, M. Foroutan, J. Theor. Comput. Chem. **13**, 1450063 (2014).
45. S.M. Fatemi, M. Foroutan, J. Iran. Chem. Soc. **12**, 1905 (2015).
46. S.M. Fatemi, M. Foroutan, J. Nanostruct. Chem. **6**, 29 (2016).
47. S.M. Fatemi, M. Foroutan, J. Iran. Chem. Soc. **14**, 269 (2017).
48. S.M. Fatemi, M. Foroutan, J. Adv. Phys. **5**, 129 (2016).
49. S.M. Fatemi, M. Foroutan, J. Colloid Sci. Biotechnol. **2**, 40 (2013).
50. X. Liu, X. Pan, S. Zhang, X. Han, X. Bao, Langmuir **30**, 8036 (2014).
51. J.C. Rasaiah, S. Garde, G. Hummer, Annu. Rev. Phys. Chem. **59**, 713 (2008).
52. A. Alexiadis, S. Kassinos, Chem. Rev. **108**, 5014 (2008).
53. Q. Chen, Q. Wang, Y.-C. Liu, T. Wu, J. Chem. Phys. **140**, 214507 (2014).
54. M.K. Tripathy, N.K. Jena, A.K. Samanta, S.K. Ghosh, K. Chandrakumar, Theor. Chem. Acc. **133**, 1 (2014).
55. Y.-g. Zheng, H.-f. Ye, Z.-q. Zhang, H.-w. Zhang, Phys. Chem. Chem. Phys. **14**, 964 (2012).
56. J.K. Clark II, S.J. Paddison, Phys. Chem. Chem. Phys. **16**, 17756 (2014).
57. S. Li, B. Schmidt, Phys. Chem. Chem. Phys. **17**, 7303 (2015).
58. B. Mukherjee, P.K. Maiti, C. Dasgupta, A. Sood, J. Chem. Phys. **126**, 124704 (2007).
59. A. Striolo, Nano Lett. **6**, 633 (2006).
60. H. Kumar, B. Mukherjee, S.-T. Lin, C. Dasgupta, A. Sood, P.K. Maiti, J. Chem. Phys. **134**, 124105 (2011).
61. B. Mukherjee, P.K. Maiti, C. Dasgupta, A. Sood, J. Phys. Chem. B **113**, 10322 (2009).
62. J.K. Holt, H.G. Park, Y. Wang, M. Stadermann, A.B. Artyukhin, C.P. Grigoropoulos, A. Noy, O. Bakajin, Science **312**, 1034 (2006).
63. J.A. Thomas, A.J. McGaughey, Nano Lett. **8**, 2788 (2008).
64. F. Taghavi, S. Javadian, S.M. Hashemianzadeh, J. Mol. Graph. Modell. **44**, 33 (2013).
65. T.A. Pascal, W.A. Goddard, Y. Jung, Proc. Natl. Acad. Sci. (U.S.A.) **108**, 11794 (2011).
66. W.H. Noon, K.D. Ausman, R.E. Smalley, J. Ma, Chem. Phys. Lett. **355**, 445 (2002).
67. D.W. Boukhvalov, M.I. Katsnelson, Y.-W. Son, Nano Lett. **13**, 3930 (2013).
68. A. Tahat, J. Martí, Phys. Rev. E **92**, 032402 (2015).
69. K.S. Novoselov, A.K. Geim, S. Morozov, D. Jiang, Y. Zhang, S.a. Dubonos, I. Grigorieva, A. Firsov, Science **306**, 666 (2004).
70. X. Li, C.W. Magnuson, A. Venugopal, R.M. Tromp, J.B. Hannon, E.M. Vogel, L. Colombo, R.S. Ruoff, J. Am. Chem. Soc. **133**, 2816 (2011).
71. R. Song, W. Feng, C.A. Jimenez-Cruz, B. Wang, W. Jiang, Z. Wang, R. Zhou, RSC Adv. **5**, 274 (2015).
72. S. Pařez, M. Pědota, Phys. Chem. Chem. Phys. **14**, 3640 (2012).
73. D.J. Bonthuis, S. Gekle, R.R. Netz, Phys. Rev. Lett. **107**, 166102 (2011).
74. Z. Zhang, P. Fenter, L. Cheng, N. Sturchio, M. Bedzyk, M. Pědota, A. Bandura, J. Kubicki, S. Lvov, P. Cummings, Langmuir **20**, 4954 (2004).
75. J. Marti, J. Sala, E. Guardia, J. Mol. Liq. **153**, 72 (2010).
76. H. Eslami, N. Heydari, J. Nanopart. Res. **16**, 1 (2014).
77. R. Guégan, J. Colloid Interface Sci. **358**, 485 (2011).
78. S.A. Deshmukh, G. Kamath, G.A. Baker, A.V. Sumant, S.K. Sankaranarayanan, Surf. Sci. **609**, 129 (2013).
79. A.A. Chialvo, L. Vlcek, P.T. Cummings, J. Phys. Chem. C **118**, 19701 (2014).
80. M. Zokaie, M. Foroutan, RSC Adv. **5**, 39330 (2015).
81. M. Zokaie, M. Foroutan, RSC Adv. **5**, 97446 (2015).
82. W.-H. Zhao, L. Wang, J. Bai, L.-F. Yuan, J. Yang, X.C. Zeng, Acc. Chem. Res. **47**, 2505 (2014).
83. M. Foroutan, S.M. Fatemi, F. Shokouh, J. Mol. Graphics Modell. **66**, 85 (2016).
84. M. Erko, G. Findenegg, N. Cade, A. Michette, O. Paris, Phys. Rev. B **84**, 104205 (2011).
85. A. Schreiber, I. Ketelsen, G.H. Findenegg, Phys. Chem. Chem. Phys. **3**, 1185 (2001).
86. J.P. Layfield, D. Troya, J. Phys. Chem. B **115**, 4662 (2011).
87. Y. Hu, D. Devegowda, A. Striolo, A. Phan, T.A. Ho, F. Civan, R. Sigal, J. Unconv. Oil Gas Res. **9**, 31 (2015).
88. D. Hou, T. Zhao, H. Ma, Z. Li, J. Phys. Chem. C **119**, 1346 (2015).
89. R. Gnanasekaran, Y. Xu, D.M. Leitner, J. Phys. Chem. B **114**, 16989 (2010).
90. M. Ding, A. Szymczyk, F. Goujon, A. Soldera, A. Ghoufi, J. Membr. Sci. **458**, 236 (2014).
91. N. Giovambattista, P.G. Debenedetti, P.J. Rossky, J. Phys. Chem. B **111**, 9581 (2007).
92. N. Choudhury, Chem. Phys. **421**, 68 (2013).
93. M. Springborg, R. Paul, G. Maroulis, B. Kirchner, S. Roy, G. Wu, P. Sarkar, A. Savin, *Chemical Modelling: Applications and Theory* (Royal Society of Chemistry, 2012).

94. G.B. Reddy, A. Madhusudhan, D. Ramakrishna, D. Ayo-dhya, M. Venkatesham, G. Veerabhadram, J. Nanostruct. Chem. **5**, 185 (2015).
95. N. Salem, Y. Abu-Lebdeh, J. Electrochem. Soc. **161**, A1593 (2014).
96. X.-X. Zhang, M. Liang, N.P. Ernsting, M. Maroncelli, J. Phys. Chem. Lett. **4**, 1205 (2013).
97. A. Nath, A. Kumar, Electrochim. Acta **129**, 177 (2014).
98. G.-T. Kim, S. Jeong, M.-Z. Xue, A. Balducci, M. Winter, S. Passerini, F. Alessandrini, G. Appetecchi, J. Power Sources **199**, 239 (2012).
99. J. Vatamanu, Z. Hu, D. Bedrov, C. Perez, Y. Gogotsi, J. Phys. Chem. Lett. **4**, 2829 (2013).
100. E. van de Ven, A. Chairuna, G. Merle, S.P. Benito, Z. Borneman, K. Nijmeijer, J. Power Sources **222**, 202 (2013).
101. Y.-H. Chang, P.-Y. Lin, S.-R. Huang, K.-Y. Liu, K.-F. Lin, J. Mater. Chem. **22**, 15592 (2012).
102. R. Gao, D. Wang, J.R. Heflin, T.E. Long, J. Mater. Chem. **22**, 13473 (2012).
103. G.K. Dedzo, S. Letaief, C. Detellier, J. Mater. Chem. **22**, 20593 (2012).
104. M. Mohammadi, M. Foroutan, J. Mol. Liq. **193**, 60 (2014).
105. Y. Luo, Q. Wang, Q. Lu, Q. Mu, D. Mao, Environ. Sci. Technol. Lett. **1**, 266 (2014).
106. N. Yaghini, J. Pitawala, A. Matic, A. Martinelli, J. Phys. Chem. B **119**, 1611 (2015).
107. R. Macfarlaned, J. Golding, S. Forsyth, Chem. Com. **16**, 1430 (2001).
108. R. Hagiwara, K. Tamaki, K. Kubota, T. Goto, T. Nohira, J. Chem. Eng. Data **53**, 355 (2008).
109. R. Göbel, P. Hesemann, J. Weber, E. Möller, A. Friedrich, S. Beuermann, A. Taubert, Phys. Chem. Chem. Phys. **11**, 3653 (2009).
110. N. Jain, A. Kumar, S. Chauhan, S. Chauhan, Tetrahedron **61**, 1015 (2005).
111. M.K. Muthayala, B.S. Chhikara, K. Parang, A. Kumar, ACS Comb. Sci. **14**, 60 (2011).
112. M.K. Muthayala, A. Kumar, ACS Comb. Sci. **14**, 5 (2011).
113. B.C. Ranu, S. Banerjee, Org. Lett. **7**, 3049 (2005).
114. A. Kumar, M.K. Muthayala, Tetrahedron Lett. **52**, 5368 (2011).
115. F. Meersman, C. Dirix, S. Shipovskov, N.L. Klyachko, K. Heremans, Langmuir **21**, 3599 (2005).
116. D. Seth, A. Chakraborty, P. Setua, N. Sarkar, Langmuir **22**, 7768 (2006).
117. K.A. Fletcher, S. Pandey, Langmuir **20**, 33 (2004).
118. M. Kanakubo, Y. Hiejima, K. Minami, T. Aizawa, H. Nanjo, Chem. Commun. (17), 1828 (2006) DOI: 10.1039/B600074F.
119. F. Shi, Y. Deng, Spectrochim. Acta A **62**, 239 (2005).
120. S. Letaief, T.A. Elbokl, C. Detellier, J. Colloid Interface Sci. **302**, 254 (2006).
121. H. Gao, J. Li, B. Han, W. Chen, J. Zhang, R. Zhang, D. Yan, Phys. Chem. Chem. Phys. **6**, 2914 (2004).
122. R. Singh, J. Monk, F.R. Hung, J. Phys. Chem. C **114**, 15478 (2010).
123. Q. Dou, M. Sha, H. Fu, G. Wu, J. Phys. Chem. C **115**, 18946 (2011).
124. S. Chen, K. Kobayashi, Y. Miyata, N. Imazu, T. Saito, R. Kitaura, H. Shinohara, J. Am. Chem. Soc. **131**, 14850 (2009).
125. S. Chen, G. Wu, M. Sha, S. Huang, J. Am. Chem. Soc. **129**, 2416 (2007).
126. M.A. Balazadeh, M. Foroutan, Fluid Phase Equilib. **356**, 63 (2013).
127. H. Akbarzadeh, M. Abbaspour, S. Salemi, S. Abdollahzadeh, RSC Adv. **5**, 3868 (2015).
128. T. Méndez-Morales, J. Carrete, M. Pérez-Rodríguez, Ó. Cabeza, L.J. Gallego, R.M. Lynden-Bell, L.M. Varela, Phys. Chem. Chem. Phys. **16**, 13271 (2014).
129. R. Singh, N.N. Rajput, X. He, J. Monk, F.R. Hung, Phys. Chem. Chem. Phys. **15**, 16090 (2013).
130. N.N. Rajput, J. Monk, R. Singh, F.R. Hung, J. Phys. Chem. C **116**, 5169 (2012).
131. N.N. Rajput, J. Monk, F.R. Hung, J. Phys. Chem. C **118**, 1540 (2014).
132. N.N. Rajput, J. Monk, F.R. Hung, J. Phys. Chem. C **116**, 14504 (2012).
133. M.V. Fedorov, R. Lynden-Bell, Phys. Chem. Chem. Phys. **14**, 2552 (2012).
134. M. Sha, G. Wu, Y. Liu, Z. Tang, H. Fang, J. Phys. Chem. C **113**, 4618 (2009).
135. C. Pinilla, M.G. Del Pópolo, R.M. Lynden-Bell, J. Kohanoff, J. Phys. Chem. B **109**, 17922 (2005).
136. Y. Shim, H.J. Kim, Y. Jung, Faraday Discuss. **154**, 249 (2012).
137. M. Alibalazadeh, M. Foroutan, J. Mol. Model. **21**, 1 (2015).
138. S. Salemi, H. Akbarzadeh, S. Abdollahzadeh, J. Mol. Liq. **215**, 512 (2016).
139. A.K. Gupta, Y.L. Verma, R.K. Singh, S. Chandra, J. Phys. Chem. C **118**, 1530 (2014).
140. G. Ori, F. Villemot, L. Viau, A. Vioux, B. Coasne, Mol. Phys. **112**, 1350 (2014).
141. G. Ori, C. Massobrio, A. Pradel, M. Ribes, B. Coasne, Langmuir **31**, 6742 (2015).
142. F.F. Canova, H. Matsubara, M. Mizukami, K. Kurihara, A.L. Shluger, Phys. Chem. Chem. Phys. **16**, 8247 (2014).
143. L.E. Ficke, J.F. Brennecke, J. Phys. Chem. B **114**, 10496 (2010).
144. W. Jiang, Y. Wang, G.A. Voth, J. Phys. Chem. B **111**, 4812 (2007).
145. M.G. Freire, C.M. Neves, P.J. Carvalho, R.L. Gardas, A.M. Fernandes, I.M. Marrucho, L.M. Santos, J.A. Coutinho, J. Phys. Chem. B **111**, 13082 (2007).
146. Y. Li, L.-S. Wang, S.-F. Cai, J. Chem. Eng. Data **55**, 5289 (2010).
147. S. Feng, G.A. Voth, Fluid Phase Equilib. **294**, 148 (2010).
148. T. Méndez-Morales, J. Carrete, O. Cabeza, L.J. Gallego, L.M. Varela, J. Phys. Chem. B **115**, 6995 (2011).
149. A.K. Gupta, M.P. Singh, R.K. Singh, S. Chandra, Dalton Trans. **41**, 6263 (2012).
150. A.K. Gupta, R.K. Singh, S. Chandra, RSC Adv. **4**, 22277 (2014).
151. A.K. Gupta, R.K. Singh, S. Chandra, RSC Adv. **3**, 13869 (2013).